Basal Mantle Flow Over LLSVPs Explains Differences in Pacific and Indo-Atlantic Hotspot Motions

A. Bellas & L. Royden

Abstract

Surface hotspot motions are approximately a factor of two faster in the Pacific than the Indo-Atlantic, and the Pacific large low shear velocity province (LLSVP) appears to be significantly shorter than the Indo-Atlantic LLSVP. Hypothesizing that surface hotspot motions are correlated with the motion of plume sources on the upper surface of chemically distinct, intrinsically dense LLSVPs, we use 3D spherical mantle convection models to compute the velocity of plume sources and compare with observed surface hotspot motions. No contrast in the mean speed of Pacific and Indo-Atlantic hotspots is predicted if the LLSVPs are treated as purely thermal anomalies and plume sources move laterally across the core-mantle boundary. However, when LLSVP topography is included in the model, the predicted hotspot speeds are, on average, faster in the Pacific than the Indo-Atlantic, even when modest topography is assigned to both LLSVPs (e.g., 100-300 km). The difference in mean hotspot speed increases to a factor of two for larger and laterally variable LLSVP topography estimated from seismic tomographic model S40RTS (up to 1100-1500 km for the Indo-Atlantic region versus 700-1400 km for the Pacific region) and our results also broadly reproduce the convergence of Pacific hotspots toward the center of the Pacific LLSVP. These largescale features of global hotspot motions are only reproduced when ambient mantle material flows over large, relatively stable topographical features, suggesting that LLSVPs are chemically distinct and intrinsically dense relative to ambient mantle material.

Key Points

1. Pacific hotspot motions are on average two times faster than Indo-Atlantic hotspots in commonly used reference frames
2. Analysis of seismic tomographic model S40RTS suggests the Indo-Atlantic LLSVP is taller than the Pacific LLSVP
3. Surface hotspot motions are reproduced in geodynamic models only if LLSVPs behave like topography that plume sources are advected over

Plain Language Summary

Seismic observations reveal two continent-sized anomalies at the base of the Earth's mantle, referred to as Large Low-Shear-Velocity Provinces, or LLSVPs, through which seismic waves travel slowly. Slow seismic velocity is generally interpreted as increased temperature. However, buoyant plumes of hot material rise from the LLSVPs and produce hotspot volcanoes on the Earth's surface, and the geochemistry of these lavas suggest that LLSVPs are primordial. To explain why the LLSVPs have remained at the base of the mantle for billions of years, they must have higher intrinsic density that the ambient mantle in addition to being hot, but this is still debated. To contribute to understanding whether LLSVPs are intrinsically dense, chemically distinct piles versus purely thermal, we compare the velocity of ambient mantle flow, which advects plume sources over LLSVPs, with surface hotspot motions. Results show that the largescale differences in surface hotspot motions are reproduced only when LLSVPs behave like topography that deflects ambient mantle flow. Since LLSVPs would only behave like topography that deflects ambient mantle flow if they are denser than ambient mantle material, our results provide additional evidence in support of LLSVPs as dense thermochemical piles.

1. Introduction

The large low shear velocity provinces (LLSVPs) are among the most robust features recovered in global seismic tomographic models of the Earth (*Dziewonski*, 1984; *Woodhouse & Dziewonski*, 1989; *Becker & Boschi*, 2002; *Ritsema et al.,* 2011; *French & Romanowicz*, 2015). In addition, most large igneous provinces and hotspot volcanoes arise from LLSVP interiors and/or peripheries, and appear to have done so for the past several hundred million years (*Burke & Torsvik*, 2004; *Torsvik et al.,* 2006). Furthermore, the geochemistry of hotspot-generated lavas suggests that LLSVPs may be the ancient, un-degassed remnants of a differentiation event that occurred early in Earth's history (e.g., 4.45 Ga) (*Castillo,* 1988; *Jackson et al*., 2010; *Mukhopadhyay*, 2012; *Harpp et al*., 2014; *Mundl et al.,* 2017; *Harrison et al.*, 2017; *Jackson et al*., 2017; *Williams et al*., 2015, 2019). As such, the LLSVPs provide fundamental constraints on the composition, dynamics, and evolution of the Earth.

Deep mantle flow driven by descending slabs has long been understood to move thermal instabilities (i.e., plume sources) across the core-mantle boundary (*Olson,* 1987), and discrete plume sources appear to also be affected by the structure of the LLSVPs (*Davaille et al.,* 2002; *Jellinek & Manga*, 2002; *McNamara & Zhong,* 2004; *Li & Zhong*, 2017). The LLSVPs may represent relatively stable, dense piles at the base of the mantle, with "topography" that interacts with flow in the surrounding mantle, potentially explaining the motion of plume sources at the base of the ambient mantle, and hotspot motions at the surface. If correct, then the study of surface hotspot motions may provide insight into the morphology and dynamic stability of the LLSVPs, and their interaction with the ambient mantle.

The Indo-Atlantic LLSVP is significantly taller than the Pacific LLSVP based on the vertical gradient of seismic velocity in a multitude of cross-sections (*Yuan & Li*, 2022), and the mean speed of Pacific hotspots (21.5 mm/yr) is a factor of two larger than that of the Indo-Atlantic hotspots (10.6 mm/yr) in the Fixed Hotspot Reference Frame (presented below). Differences in Indo-Atlantic and Pacific LLSVP topography, and their location relative to major subduction zones, might explain some of the differences in the associated hotspot motions. We hypothesize that the slow lateral motion of the Indo-Atlantic hotspots may be due to the taller and steeper topography of the Indo-Atlantic LLSVP which impedes the lateral motion of plume sources. Meanwhile, the more rapid and convergent motion of the Pacific hotspots may be correlated with the smaller LLSVP topography and, in part, with mantle flow related to descending slab material. In this paper, we investigate how large scale mantle convection may interact with stable LLSVPs to influence plume source motion and surface hotspot motion using 3D-spherical models of mantle convection and a variety of estimates of LLSVP topography.

2. Observed Hotspot Motions

The present-day motions of 34 hotspots are estimated from the observed azimuth and rate of hotspot tracks over the past 5-10 Ma (*Morgan & Phipps-Morgan*, 2007). Of these 34 hotspots, 29 are of deep mantle origin based on geochemical and seismic evidence (*Jackson et al*., 2018). We neglect the remaining five hotspots which are located near the Pacific-North American plate boundary (Bowie, Cobb, Yellowstone, Guadalupe, and Raton).

An individual hotspot's motion is estimated relative to the plate it pierces, and to reference all hotspot motions relative to a common reference frame, we subtract the respective plate motion in the No-Net-Rotation reference frame (NNR; *DeMets et al.,* 2010; *Argus et al.,* 2011) from each hotspot. This gives

$$\vec{v}_{hotspot}^{(NNR)} = \vec{v}_{hotspot}^{(plate)} - \vec{v}_{plate}^{(NNR)}, \tag{1}$$

where subscripts and superscripts denote what is moving relative to what, respectively. The average speed of the 29 hotspots relative to NNR is 22.5 ± 13.5 mm/year overall, or 29.2 ± 14.9 mm/year in the Pacific, and 15.7 ± 7.8 mm/year in the and Indo-Atlantic (Figure 1a).

The Fixed Hotspot Reference Frame (FHRF) is defined as the rigid body rotation which minimizes the sum of residual hotspot motions. Consider an arbitrary rotation vector with origin located at the center of the Earth and unit length, $\hat{p}_i$ (i.e., a pole). The velocity associated with this rotation, $\Delta\vec{v}_{\mathrm{ij}}^{(0)}$, is given by the cross product with a position vector, $\vec{r}_j$ (e.g., for each hotspot, *j*),

$$\Delta\vec{v}_{\mathrm{ij}}^{(0)} = \hat{p}_i \otimes \vec{r}_j. \tag{2}$$

Hotspot velocities in the reference frame defined by $\hat{p}_i$ can be expressed by subtracting the velocity of rotation

$$\vec{v}_j^{(i)} = \vec{v}_j^{(NNR)} - \Delta\vec{v}_{\mathrm{ij}}^{(0)}, \tag{3}$$

where $\vec{v}_j^{(NNR)}$ is the velocity of each hotspot (*j*) relative to NNR (i.e., equation 1). This can then can be generalized for a pole of arbitrary rotation rate, $\vec{p}_i = \omega_i\hat{p}_i$,

$$\vec{v}_j^{(i)} = \vec{v}_j^{(NNR)} - \omega_i\Delta\vec{v}_{\mathrm{ij}}^{(0)}. \tag{4}$$

We now have an expression that is general in terms of the position of the pole (*i*) and its length (ω_i). We will first solve ω_i for a given pole position by minimizing the sum of the hotspot motion residuals

$$R = \sum_{j=1}^{N_{hotspots}} \left(\vec{v}_j^{(NNR)} - \omega_i \Delta\vec{v}_{\mathrm{ij}}^{(0)}\right)^2. \quad (5)$$

The minimum of equation (5) is given by

$$\frac{\partial R}{\partial \omega} = 0 = \sum_{j=1}^{N_{hotspots}} 2\left(\vec{v}_j^{(NNR)} - \omega_i \Delta\vec{v}_{\mathrm{ij}}^{(0)}\right) \cdot \left(-\Delta\vec{v}_{\mathrm{ij}}^{(0)}\right), \quad (6)$$

which simplifies to

$$\omega_i = \frac{\sum_{j=1}^{N_{hotspots}} \vec{v}_j^{(NNR)} \cdot \Delta\vec{v}_{\mathrm{ij}}^{(0)}}{\left(\Delta\vec{v}_{\mathrm{ij}}^{(0)}\right)^2}. \quad (7)$$

We first solve ω_i for each pole position $\hat{p}_i$ on a coarse 3ºx3º grid. We then iterate about the best fit pole on local, refined grids of ±10º and 1ºx1º resolution, then ±2.5º and 0.25ºx0.25º resolution, and finally ±0.05º and 0.005ºx0.005º resolution.

The resulting pole of the FHRF is defined by coordinates 256.8 ºE, 46.8 ºN, and a rotation rate of 0.167 º/Myr relative to NNR. The mean residual hotspot motions are 16.7 ± 12.9 mm/year overall, or 21.5 ±12.7 mm/year in the Pacific, and 10.6 ± 9.8 mm/year in the Indo-Atlantic (Figure 1b). In both the FHRF and NNR, the velocity of the Pacific hotspot motions are faster than Indo-Atlantic hotspot motions by a factor of ~2 on average, have a greater scatter by a factor of ~1.6, and Pacific hotspots converge toward the central Pacific (Figure 1).

In the following sections, we compute velocities in the deep mantle for a variety of LLSVP morphologies. Assuming that hotspot motions are correlated with plume source motions at the base of the mantle, we use these results to constrain the dynamic effects of the LLSVPs on large-scale basal mantle flow. We will show that some of the large-scale features of observed hotspot motions may be caused, under certain conditions, by buoyancy-driven flow in the ambient mantle interacting with the topography of intrinsically dense piles or LLSVPs.

3. Methods and Model Setup

We use 3D-spherical, instantaneous thermal convection models to investigate how basal flow over LLSVPs might affect surface hotspot motions via the motion of hotspot source regions. We solve the velocity field from the conservation equations of mass, momentum, and energy in the Boussinesq approximation using CitcomS (*Zhong et al.,* 2008). The buoyancy field is derived from the seismic tomographic model S40RTS converted to temperature with a uniform scaling factor equal to 0.035 and

mean nondimensional temperature equal to 0.5196. We consider viscosity structures that are either purely layered or layered and temperature-dependent with a factor of 60 increase in viscosity at 660 km depth (Table 1), plus addition modification to viscosity in the LLSVPs (see below). Temperature-dependent viscosity is assigned following the Arrhenius form $\eta = \eta_0 \exp\left(\frac{E}{RT}\right)$ with activation energy, *E,* set to 120 kJ/mol (e.g., *Bellas et al.*, 2018). We set the upper mantle viscosity equal to 4.2×10^{20} Pa s and lower mantle viscosity to 2.5×10^{22} Pa s (e.g., Mao et al., 2021).

The finite element grid, which spans a nondimensional radius 0.55 to 1.0, is divided into 12 spherical caps, each with 81 vertical nodes and 65 horizontal nodes. Vertical grid refinement is applied in the lower mantle to produce grid resolution equal to ~30 km up to ~1400 km above the core-mantle boundary (CMB) to resolve flow over the LLSVP surfaces (i.e., plume source motions). Models are instantaneous such that the velocity field represents present-day flow in the mantle based on the present-day buoyancy structure. Surface and bottom boundary conditions are free-slip.

In addition to reference models without LLSVPs (Case 0a and Case 0b), the model setup contains stable LLSVPs at the base of the mantle, with LLSVP topography (height above the CMB) determined from S40RTS. Low topography, or "deflated", dense-cored LLSVPs are supported by a recent study (*Richards et al.,* 2023), while taller LLSVP topography is suggested by another (*Yuan & Li*, 2022). Following *Richards et al.* (2023), cases 1-3 are formulated with low-topography LLSVPs that have lateral extent defined by regions at the base of the mantle where seismic velocity is slower than average (Figure 2c; Figure 3c-d). In these regions, the LLSVP topography is uniform and set equal to 100 km for Case 1a and Case 1b, to 200 km for Case 2a and Case 2b, and to 300 km for Case 3a and Case 3b (viscosity is purely layered in cases ending with "-a", and viscosity is layered and temperature-dependent in cases ending with "-b").

In order to stabilize the LLSVPs, we artificially increase the viscosity of material within the LLSVPs by an amount sufficient to retard flow within the LLSVPs. For the purely layered viscosity cases, an increase in viscosity by a factor of 10 is sufficient to stabilize the LLSVPs. For the temperature-dependent viscosity cases, an increase in LLSVP viscosity by a factor of 100 is needed to stabilize the LLSVP material (Figure 2). Note that this is not an assertion that LLSVPs have a high viscosity, but only that we use viscosity as a proxy to test the dynamical effects of relatively stable and intrinsically dense material on the buoyancy-driven flow of ambient mantle material.

We also examine cases in which LLSVP topography is laterally variable. We estimate the topography of the LLSVPs by computing a 300 km radial-moving-window-average of S40RTS,

$dv_S^{(300km)}(\theta,\phi,r)$ because this approach prevents the identification of the LLSVP surface with small-scale perturbations in S40RTS. Searching upward from the CMB, we estimate the position of the upper surface of the LLSVP as the location where $dv_S^{(300km)}$ first becomes faster than a threshold value. The seismic velocity threshold that defines the upper surface of the LLSVPs is -1.0% (Case 4a and Case 4b), and -0.75% (Case 5a and Case 5b). This method of estimating LLSVP topography produces two distinct piles which reach a maximum height of ~700 km in the Pacific and ~1100 km in the Indo-Atlantic (Case 4a and Case 4b) and ~1400 km in the Pacific and ~1500 km in the Indo-Atlantic (Case 5a and Case 5b). These differences in height are substantially smaller than those estimated by *Yuan & Li* (2022) who considered the vertical gradient in dv_S.

We compare the predicted velocity of ambient mantle material over the LLSVP surfaces to observed present-day hotspot motions assuming (i) that the lateral motions of plume sources are driven, at least in part, by the flow of ambient mantle material, (ii) that basal flow in the mantle is relatively stable over the last ~30 Ma (i.e., mantle transit time), and (iii) that velocities in the mid-mantle are dominantly vertical. We consider all of these assumptions to be reasonable, but because they are approximate in nature, and because of the large uncertainties associated with converting S40RTS to buoyancy, we do not expect precise agreement between our predictions and the observations. Our aim is to reproduce large-scale features of the observations.

We choose to impose stability of the LLSVPs rather than employing thermochemical mantle convection models because the ratio of thermal to compositional buoyancy in the LLSVPs is poorly constrained, not to mention time-dependent. In addition, thermochemical convection models with imposed surface plate motion over the past 80 Ma have already been investigated by *Li & Zhong* (2019), and they did not reproduce the factor of 2 contrast in mean hotspot speeds between the Pacific and Indo-Atlantic. Rather than introduce unknown parameters to the models, we choose to simulate the dynamic effects of LLSVPs as stable piles by increasing their viscosity. It is important to note that the large temperature inferred from the slow seismic velocity of LLSVPs would suggest that they are, in reality, of lower viscosity than the ambient mantle, in which case their stability would be caused by other thermodynamic properties (e.g., excess density associated with their chemical composition). The present study also neglects boundary layer dynamics, and it is not clear how this can be reliably improved given the relatively low resolution of seismic tomographic models and uncertainty in thermodynamic properties of the deep mantle (e.g., rheology, compositional and thermal buoyancy).

4. Results

We begin with reference cases that treat LLSVPs as purely thermal anomalies. In Case 0a, model results show divergent flow at the base of the mantle away from centers of negative buoyancy related to subduction beneath the Middle East, Tibet, the Andes, and the Farallon slab region. This results in convergent basal flow in the Indo-Atlantic LLSVP that is equal in strength to that in the Pacific LLSVP, despite the close proximity of circum-Pacific subduction zones to the Pacific LLSVP (Figures 2a,b and 3a). If basal flow velocities are correlated with surface hotspot motions, then these results disagree with the observed behavior of hotspots in the two domains. The average predicted speeds at hotspot locations in the Pacific and Indo-Atlantic are 38 mm/year and 37 mm/year, respectively, which fail to reproduce the factor of two contrast in observed speeds and significantly overestimate them in both domains (21.5 mm/year and 10.6 mm/year; Table 1). The agreement with observations is further degraded if temperature-dependent viscosity is introduced in Case 0b, where the mean predicted hotspots speeds increase to 48.4 mm/year and 50.6 mm/year in the Pacific and Indo-Atlantic, respectively, such that Indo-Atlantic hotspots move even faster than Pacific hotspots in this case (Figure 2a,c; Figure 3b).

In Cases 1a and 1b, we introduce LLSVPs as topographical features that ambient mantle material flows over. LLSVP topography is assigned to be uniform and equal to 100 km in any region where seismic velocity is slower than average at the base of the mantle (Figure 2d,e,f; Figure 3c,d). The viscosity is increased by a factor of 10 inside the LLSVPs in Case 1a with otherwise purely layered viscosity (Figure 2d), and by a factor of 100 in Case 1b with layered and temperature-dependent viscosity (Figure 2e). The effect of introducing stable 100 km-high topographic features at the base of the mantle is to reduce the magnitude of basal flow velocity over the Indo-Atlantic LLSVP to a greater degree than the Pacific LLSVP (Figure 3c,d). In Case 1a, the predicted average hotspot speeds are 29.5 mm/year and 22.9 mm/year in the Pacific and Indo-Atlantic regions, respectively, and in Case 1b they are 23.4 mm/year and 18.1 mm/year (Table 1). Most importantly, the predicted average speed of Pacific hotspots is a factor of 1.3 greater than that of the Indo-Atlantic hotspots for Cases 1a and 1b. While this underestimates the observed ratio of 2.0, the predictions do agree better with the observations than Case 0a and Case 0b with no LLSVP topography.

In Case 2a and Case 2b, LLSVP topography is increased to 200 km but all else is the same (Figure 2g,h,i). The predicted average speeds of hotspots in Case 2a are 23.5 mm/year and 17.5 mm/year in the Pacific and Indo-Atlantic regions, respectively, and in Case 2b they are 12.0 mm/year and 10.1 mm/year, respectively (Table 1; Figure 3e,f). The predicted ratios of Pacific to Indo-Atlantic hotspot average speeds

are 1.3 in Case 2a, and 1.2 in Case 2b. In Case 3a and Case 3b, LLSVP topography is increased to 300 km but all else is the same (Figure 2j,k,l). The mean predicted hotspot speeds are 20.8 mm/year and 15.6 mm/year in the Pacific and Indo-Atlantic in Case 3a, and 8.5 mm/year and 8.2 mm/year in Case 3b (Table 1; Figure 3g,h). The ratio of Pacific to Indo-Atlantic hotspot speeds are 1.3 and 1.0, respectively. Overall, it appears that compact, uniform topography LLSVPs produce a ratio of Pacific to Indo-Atlantic hotspots between 1.0 and 1.3, which is significantly smaller than the observed ratio, but a general improvement relative to cases with no LLSVP topography.

Next, we use the 300 km radial-moving-window-average of S40RTS, $dv_S^{(300km)}(\theta,\phi,r)$, to investigate the effects of larger and laterally variable LLSVP topography (Figure 4,5). In both Case 4a and Case 4b, the maximum LLSVP topography is equal to 700 km in the Pacific and 1100 km in the Indo-Atlantic. Case 4a predicts mean hotspot speeds in the Pacific and Indo-Atlantic are 28.3 mm/year and 18.6 mm/year, respectively. For Case 4b, the corresponding model speeds are 32.9 and 15.6 mm/year. The ratio of Pacific to Indo-Atlantic mean speed increase to 1.5 in Case 4a, and 2.1 in Case 4b, in very good agreement with the observations.

For Case 5a, with maximum LLSVP topography equal to 1400 km and 1500 km the Pacific and Indo-Atlantic, respectively, the mean model hotspot speeds are 21.7 mm/year and 15.0 mm/year in the Pacific and Indo-Atlantic, respectively (Figure 5c). For Case 5b, they are 19.6 mm/year and 10.5 mm/year, respectively (Figure 5d). The ratio of Pacific to Indo-Atlantic mean speed is 1.4 in Case 5a and 1.9 in Case 5b, also in very good agreement with observations. In general, the factor of two contrast in observed hotspot speeds is best reproduced by cases with large, laterally variable LLSVP topography, and temperature-dependent viscosity (i.e., Case 4b and Case 5b).

Figure 6 shows the average speeds of the Pacific and Indo-Atlantic hotspots, as computed in each model, and the ratio of Pacific to Indo-Atlantic mean hotspot speeds. Ultimately, Case 5b with temperature dependent viscosity and LLSVP topography defined by $dv_S^{(300km)}$<-0.75% reproduces these observations best. However, Case 4b reproduces the ratio of Pacific to Indo-Atlantic mean speeds of ~2, and thus is comparably successful in explaining the more rapid mean speed of the Pacific hotspots.

In Figure 7, hotspot speeds are binned by 10 mm/year increments and shown as a distribution for the Pacific (left panels) and Indo-Atlantic (right panels) domains. Most Indo-Atlantic hotspots move with observed speeds of less than 10 mm/year, while most observed Pacific hotspot speeds are distributed between 10 and 30 mm/year (Figure 7). Overall, Case 5a and Case 5b best-reproduce the distribution of hotspot speeds, and Case 4a and Case 4b agree with observations fairly well too.

Cases with large and laterally variable LLSVP topography generally reproduce the observed rapid convergence toward the south-central Pacific (Figure 8), and we observe a consistent reduction in the sum of convergent velocities in the Indo-Atlantic as LLSVP topography is increased from Case 1a to Case 5b (Figure 9a), which represents a steady improvement in agreement with observations. Ultimately, it is only Case 5a and Case 5b that reproduce the modest divergence of Indo-Atlantic hotspots, and therefore the negative ratio of convergent velocities in the Pacific relative to the Indo-Atlantic (Figure 9b).

5. Discussion

In the present study, we sought to test whether the largescale features of surface hotspot motions can be explained by basal flow over LLSVPs. The key results of our study are

(i) that the factor of 2 contrast in observed mean hotspot speeds between the Pacific versus Indo-Atlantic is not reproduced by model predictions if LLSVPs are treated as purely thermal anomalies,

(ii) that if LLSVPs are treated as topographical features that ambient mantle must flow over, then even small topography (e.g., 100-300 km above the CMB) is capable of reducing the mean hotspot speed in the Indo-Atlantic while maintaining larger mean speeds in the Pacific, and

(iii) that the observed contrast in hotspot speeds is reproduced only in cases where LLSVP topography is large (>=700 km) and laterally variable (e.g., estimated from S40RTS as height at which $dv_S^{(300km)}$<-0.75%, or $dv_S^{(300km)}$<-1.0%).

In particular, Case 5b best-reproduced the observed mean hotspot speeds, the factor of 2 ratio between the mean speed of Pacific and Indo-Atlantic hotspots (Figure 5, Figure 6), the general distribution of hotspot speeds within each region (Figure 7), and the convergent velocity pattern in the Pacific and Indo-Atlantic (Figure 8, Figure 9). Individual hotspot motions are not well-reproduced by any of the models, but the residual speeds scale with the predicted speeds (Figure 10), suggesting that there is an effectively random contribution to the velocities of individual hotspot sources, which is perhaps a reflection of local topography or other features at individual plume sources, or boundary layer dynamics. The result that the observed large-scale features of surface hotspot motions can be explained by basal flow over topographical features in the lowermost mantle contributes additional evidence in support of LLSVPs as dense thermochemical piles, which are relatively dense and stable compared to ambient mantle material.

Our results favor tall, steep-sided LLSVPs (e.g., Cases 4-5) over relatively flat, deflated ones (e.g., Cases 1-3) on the basis that the factor of 2 contrast in hotspot speeds is only reproduced by the models

that include tall LLSVPs. Our analysis of S40RTS (that is, the radius at which $dv_S^{(300km)}$ first becomes faster than -1.0% or -0.75%) predicts a maximum height of the Indo-Atlantic LLSVP that is taller than that of the Pacific LLSVP by ~100-400 km. We suggest that larger and steeper topography of the Indo-Atlantic LLSVP hinders lateral motion of plume sources at the base of the mantle and partially explains the slower mean speed of hotspot in the Indo-Atlantic.

Chemically distinct and intrinsically dense LLSVPs are consistent with geodynamic observables including the geoid, dynamic topography, and CMB ellipticity, when LLSVP topography is less than ~200 km at spherical harmonic degree 2 based on instantaneous convection models (*Richards et al.,* 2023). In our models, the degree-2 spherical harmonic component of LLSVP topography has an amplitude that is less than 200 km and concordant *Richards et al.* (2023) in all cases except for Case 5a and Case 5b, for which it is 375 km. However, we note that Case 4b reproduced the ratio of mean hotspot speeds between the Pacific and Indo-Atlantic domains as well as Case 5b, and, with a reasonable increase in the viscosity could equally well reproduce the absolute velocities in each domain. In addition, it is likely that there may be vertical gradients in the density structure of the LLSVPs (e.g., *Tan & Gurnis,* 2005), such that the height of the LLSVPs determined in this study may overestimate the vertical distribution of high density material within them. In other words, the seismically-determined height of the LLSVPs might be significantly greater than that of the denser material within the LLSVP, as was also suggested by *Yuan & Li* (2023).

Time-dependent models of thermochemical convection have shown that LLSVPs with maximum topography ~600 km can be dynamically stable on geologic timescales and consistent with present-day geodynamic observables (*Liu & Zhong*, 2015). While the maximum LLSVP topography in our best-fit Cases 4-5 exceeds 600 km, it is yet to be determined whether such topography is consistent with present-day geodynamic observables, and there are tradeoffs between the initial volume of the chemically distinct material, intrinsic density contrast, and the longevity of LLSVP survival (*Yuan & Li*, 2023). At present, there are large uncertainties in and the thermodynamic properties of the LLSVPs and deep ambient mantle material that make it difficult to rule out tall chemically distinct piles (e.g., the viscosity contrast, compositional and thermal buoyancy contrasts, time-dependence).

The geometry and maximum topography of the LLSVPs that we obtain from S40RTS yields different results from the analysis of *Yuan and Li* (2022), who concluded that the Indo-Atlantic LLSVP is taller than that of the Pacific by 1000 km based on many seismic tomographic models. In order to investigate the effect that such a geometry would have on hotspot speeds, we ran one additional model,

with Pacific and Indo-Atlantic LLSVP topography set to uniformly 500 km and 1500 km, respectively (Figure 11). The predicted mean hotspot speeds for this geometry are 17.8 and 8.1 mm/year, for purely layered viscosity, or 21.8 and 8.9 mm/year for temperature-dependent viscosity, in the Pacific and Indo-Atlantic, respectively. The results give mean speed ratios of 2.2 or 2.4, which exceed the observed ratio of 2.0. Such large, chemically distinct, and intrinsically dense LLSVPs are likely not compatible with geodynamic observables (*Richards et al.,* 2023; *Liu & Zhong,* 2019), and exceed estimates of LLSVP material occupying 8% of mantle volume (*Cottar & Lekic*, 2016), but serve to demonstrate the efficacy of LLSVP topography in reproducing a contrast in Pacific to Indo-Atlantic hotspot speeds.

A previous study imposed surface plate motion history over 80 Myr in time-dependent thermochemical convection models including dense LLSVPs, and produced statistically similar hotspot motions in the Pacific and Indo-Atlantic (*Li & Zhong*, 2019). We suggest that the large-scale features of hotspot motions are sensitive to the present-day buoyancy field and morphology of LLSVPs, which are not necessarily reproduced by time-dependent models of mantle flow. Our results also differ from those of *Steinberger & O'Connell* (1998) who employed the propagator matrix method and therefore neglected all lateral gradients in viscosity.

Finally, recent studies of Stoneley modes (i.e., normal modes on the CMB) appear to rule out the possibility of dense LLSVPs with topography that exceeds 100-200 km (Koelemeijer et al. 2017), but it is yet to be seen whether the incorporation of full mode coupling will significantly alter this conclusion (*Robson et al.,* 2022). In summary, chemically distinct and intrinsically dense LLSVPs with topography as in Cases 4-5 appear to be concordant with, or, at least, reconcilable with previous studies by *Richards et al.* (2023), *Liu & Zhong* (2015) and *Koelemeijer et al*. (2017).

6. Conclusions

In this study, we sought to investigate whether the largescale features of surface hotspot motions can be explained by basal flow over topographic features in the deep mantle. Given that LLSVPs are expected to behave like topographic features if they are dense and stable thermochemical piles, but not if they are purely thermal, our results have implications for the composition and buoyancy structure of LLSVPs. We used 3D spherical models of instantaneous thermal convection and applied a scaling factor to the viscosity within LLSVPs so that they would behave like stable topographic features that ambient mantle material flows over. When LLSVPs are treated as purely thermal, the predicted mean hotspot speed in the Pacific is approximately equal to that of the Indo-Atlantic. In contrast, when LLSVPs are treated like stable topographic features that ambient mantle material must flow over, basal velocity projected from the

LLSVP surface to the Earth's surface at hotspot locations reproduces the large-scale observation that mean hotspot speeds are a factor of 2 faster in the Pacific than in the Indo-Atlantic. Based on this finding, we conclude that surface hotspot motions present evidence in support of LLSVPs as tall (>700 km) thermochemical anomalies that are denser than ambient mantle material, and that ambient mantle flows over these topographic features at the base of the mantle. We suggest that future studies consider the vertically integrated effects of lateral mantle flow on hotspot motion, as well as potential offset in location between the hotspot source and surface expression of the hotspot due to flow within the intervening mantle.

Acknowledgements

We are grateful to reviewers for constructive comments.

Data Availability Statement

The hotspot motion data and seismic tomographic model data are publicly available via the listed sources, and the mantle convection software CitcomS is publicly available through CIG.

References

Argus, D. F., R. G. Gordon, & C. DeMets (2011), Geologically current motion of 56 plates relative to the no‐net‐rotation reference frame, Geochem. Geophys. Geosyst., 12, Q11001, doi:10.1029/2011GC003751.

Becker, T. W., & Boschi, L. (2002). A comparison of tomographic and geodynamic mantle models. Geochemistry, Geophysics, Geosystems, 3(1). https://doi.org/10.1029/2001gc000168

Becker, T. W., Schaeffer, A. J., Lebedev, S., & Conrad, C. P. (2015). Toward a generalized plate motion reference frame. Geophysical Research Letters, 42(9), 3188–3196.

Burke, K., & Torsvik, T. H. (2004). Derivation of Large Igneous Provinces of the past 200 million years from long-term heterogeneities in the deep mantle. Earth and Planetary Science Letters, 227(3), 531–538. https://doi.org/10.1016/j.epsl.2004.09.015

Castillo, P. (1988), The Dupal anomaly as a trace of the upwelling lower mantle, Nature, 336, 667-670.

Cottaar, S. & Lekic (2016), V. Morphology of seismically slow lower-mantle structures. Geophys. J. Int. 207, 1122–1136.

Davaille, A., F. Girard, & M. Le Bars (2002), How to anchor hotspots in a convecting mantle? Earth Planet. Sci. Lett. 203, 621 – 634.

DeMets, C., R.G. Gordon, & D.F. Argus, (2010), Geologically Current Plate Motions, Geophysical Journal International 181 (1): 1–80.

Dziewonski, A. M. (1984). Mapping the lower mantle: Determination of lateral heterogeneity in P velocity up to degree and order 6. Journal of Geophysical Research, 89(B7), 5929–5952.

French, S. W., & Romanowicz, B. (2015). Broad plumes rooted at the base of the Earth's mantle beneath major hotspots. Nature, 525(7567), 95–99.

Harpp, K. S., Hall, P. S., & Jackson, M. G. (n.d.). Galápagos and Easter: A Tale of Two Hotspots. https://www.researchgate.net/publication/267981733

Harrison, L.N., D. Weis, & M.O. Garcia (2017), The link between Hawaiian mantle plume composition, magmatic flux, and deep mantle geodynamics, Earth and Planetary Science Letters, Volume 463, Pages 298-309, ISSN 0012-821X, https://doi.org/10.1016/j.epsl.2017.01.027.

Jackson, M. G., Becker, T. W., & Konter, J. G. (2018). Evidence for a deep mantle source for EM and HIMU domains from integrated geochemical and geophysical constraints. Earth and Planetary Science Letters, 484, 154–167. https://doi.org/10.1016/j.epsl.2017.11.052

Jackson, M. G., Carlson, R. W., Kurz, M. D., Kempton, P. D., Francis, D., & Blusztajn, J. (2010). Evidence for the survival of the oldest terrestrial mantle reservoir. Nature, 466(7308), 853–856. https://doi.org/10.1038/nature09287

Jackson, M. G., Konter, J. G., & Becker, T. W. (2017). Primordial helium entrained by the hottest mantle plumes. Nature, 542(7641), 340–343. https://doi.org/10.1038/nature21023

Jellinek, A.M., & M. Manga (2002). The influence of a chemical boundary layer on the fixity, spacing and lifetime of mantle plumes. Nature, 418, 760-763.

Koelemeijer, P., Deuss, A. & Ritsema, J. (2017), Density structure of Earth's lowermost mantle from Stoneley mode splitting observations. Nat Commun 8, 15241. https://doi.org/10.1038/ncomms15241

Li, M., & Zhong, S. (2017). The source location of mantle plumes from 3D spherical models of mantle convection. Earth and Planetary Science Letters, 478, 47–57. https://doi.org/10.1016/j.epsl.2017.08.033

Li, M., & Zhong, S. (2019). Lateral Motion of Mantle Plumes in 3-D Geodynamic Models. In Geophysical Research Letters (Vol. 46, Issue 9, pp. 4685–4693). https://doi.org/10.1029/2018gl081404

Liu, X., and S. Zhong (2015), The long-wavelength geoid from three-dimensional spherical models of thermal and thermochemical mantle convection, J. Geophys. Res. Solid Earth, 120, 4572–4596, doi:10.1002/ 2015JB012016.

McNamara, A. K., & Zhong, S. (2004). The influence of thermochemical convection on the fixity of mantle plumes. Earth and Planetary Science Letters, 222(2), 485–500. https://doi.org/10.1016/j.epsl.2004.03.008

Molnar, P., & Stock, J. (1987). Relative motions of hotspots in the Pacific, Atlantic and Indian Oceans since late Cretaceous time. Nature, 327(6123), 587–591.

Morgan, W. J., J. Phipps-Morgan, (2007). Plate velocities in the hotspot reference frame. In Special Paper 430: Plates, Plumes and Planetary Processes (pp. 65–78). https://doi.org/10.1130/2007.2430(04)

Morgan, W.J. (1971). Convection Plumes in the Lower Mantle. Nature, 230, 42-43.

Morgan, W.J. (1972). Deep Mantle Convection Plumes and Plate Motions. The American Association of Petroleum Geologists Bulletin, V. 56, No. 2, 203-213.

Mukhopadhyay, S. (2012). Early differentiation and volatile accretion recorded in deep-mantle neon and xenon. Nature, 486(7401), 101–104. https://doi.org/10.1038/nature11141

Müller, R. D., Cannon, J., Qin, X., Watson, R. J., Gurnis, M., Williams, S., et al. (2018), GPlates: Building a virtual Earth through deep time. Geochemistry, Geophysics, Geosystems, 19. doi:10.1029/2018GC007584.

Müller, R. D., Zahirovic, S., Williams, S. E., Cannon, J., Seton, M., Bower, D. J., Tetley, M. G., Heine, C., Le Breton, E., Liu, S., Russell, S. H. J., Yang, T., Leonard, J., & Gurnis, M. (2019). A global plate model including lithospheric deformation along major rifts and orogens since the Triassic. Tectonics, 38(6), 1884–1907.

Mundl, A., Touboul, M., Jackson, M. G., Day, J. M. D., Kurz, M. D., Lekic, V., Helz, R. T., & Walker, R. J. (2017). Tungsten-182 heterogeneity in modern ocean island basalts. Science, 356(6333), 66–69. https://doi.org/10.1126/science.aal4179

Olson, P. (1987). Drifting mantle hotspots. Nature, 327(6123), 559–560. https://doi.org/10.1038/327559a0

Richards, F.D., M. J. Hoggard, S. Ghelichkhan, P. Koelemeijer, H.C.P. Lau (2023), Geodynamic, geodetic, and seismic constraints favour deflated and dense-cored LLVPs, Earth and Planetary Science Letters, Volume 602, 117964, ISSN 0012-821X, https://doi.org/10.1016/j.epsl.2022.117964.

Ritsema, J., A. Deuss, H. J. van Heijst, J. H. Woodhouse (2011), S40RTS: a degree-40 shear-velocity model for the mantle from new Rayleigh wave dispersion, teleseismic traveltime and normal-mode splitting function measurements, Geophysical Journal International, Volume 184, Issue 3, Pages 1223–1236, https://doi.org/10.1111/j.1365-246X.2010.04884.x

Robson, A., H.C.P. Lau, P. Koelemeijer, B. Romanowicz (2022), An analysis of core–mantle boundary Stoneley mode sensitivity and sources of uncertainty, Geophysical Journal International, Volume 228, Issue 3, Pages 1962–1974, https://doi.org/10.1093/gji/ggab448

Steinberger, B., R. J. O'Connell (1998), Advection of plumes in mantle flow: implications for hotspot motion, mantle viscosity and plume distribution, Geophysical Journal International, Volume 132, Issue 2, Pages 412–434, https://doi.org/10.1046/j.1365-246x.1998.00447.x

Tan, E. & M. Gurnis, (2005), Metastable Superplumes and Mantle Compressibility, Geophysical Research Letters 32 (20). https://doi.org/10.1029/2005gl024190.

Torsvik, T. H., Smethurst, M. A., Burke, K., & Steinberger, B. (2006). Large igneous provinces generated from the margins of the large low-velocity provinces in the deep mantle. Geophysical Journal International, 167(3), 1447–1460. https://doi.org/10.1111/j.1365-246X.2006.03158.x

Williams, C. D., Li, M., McNamara, A. K., Garnero, E. J., & van Soest, M. C. (2015). Episodic entrainment of deep primordial mantle material into ocean island basalts. Nature Communications, 6, 8937. https://doi.org/10.1038/ncomms9937

Williams, C. D., Mukhopadhyay, S., Rudolph, M. L., & Romanowicz, B. (2019). Primitive helium is sourced from seismically slow regions in the lowermost mantle. Geochemistry, Geophysics, Geosystems, 20(8), 4130–4145. https://doi.org/10.1029/2019gc008437

Wilson, J.T. (1963). A possible origin of the Hawaiian Islands. Canadian Journal of Physics. Volume 41, 863-870.

Woodhouse, J.H., & A.M. Dziewonski (1989). Seismic modelling of the Earth's large-scale three-dimensional structure, Phil. Trans. R. Soc. Lond. A 328, 291-308.

Yuan, Q., & Li, M. (2022). Instability of the African large low-shear-wave-velocity province due to its low intrinsic density. Nature Geoscience, 15(4), 334–339. https://doi.org/10.1038/s41561-022-00908-3

Zhong, S., McNamara, A., Tan, E., Moresi, L., & Gurnis, M. (2008). A benchmark study on mantle convection in a 3-D spherical shell using CitcomS. Geochemistry, Geophysics, Geosystems, 9(10). https://doi.org/10.1029/2008gc002048

Table 1.

Case	LLSVP topography	$\eta_0^{(LLSVP)}$ [Pa s]	E [kJ/mol]	Avg speed (Pacific) [mm/year]	Avg speed (Indo-Atlantic) [mm/year]
0a	None	-	0	37.8	37.0
0b			120	48.4	50.6
1a	100 km	10	0	29.5	22.9
1b		100	120	23.4	18.1
2a	200 km	10	0	23.5	17.5
2b		100	120	12.0	10.1
3a	300 km	10	0	20.8	15.6
3b		100	120	8.5	8.2
4a	$dv_S^{(300km)}$<-1.0%	10	0	28.3	18.6
4b		100	120	32.9	15.6
5a	$dv_S^{(300km)}$<-0.75%	10	0	21.7	15.0
5b		100	120	19.6	10.5

*The observed average speeds of hotspots in the Pacific and Indo-Atlantic are 21.5 mm/year and 10.6 mm/year, respectively, in the Fixed Hotspot Reference Frame. Mean hotspot speeds are projected from basal velocity at the first node with radius greater than the local LLSVP surface.

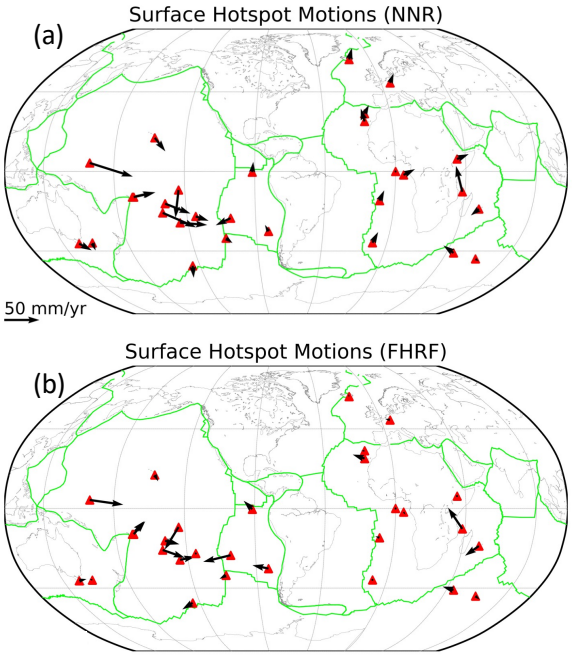

Figure 1. Surface hotspot motions relative to (a) the no-net-rotation reference frame (NNR) which is defined by surface plate motions, and (b) the Fixed Hotspot Reference Frame (FHRF). Regardless of the chosen reference frame, the observations exhibit rapid convergence in the Pacific and relative fixity in the Indo-Atlantic.

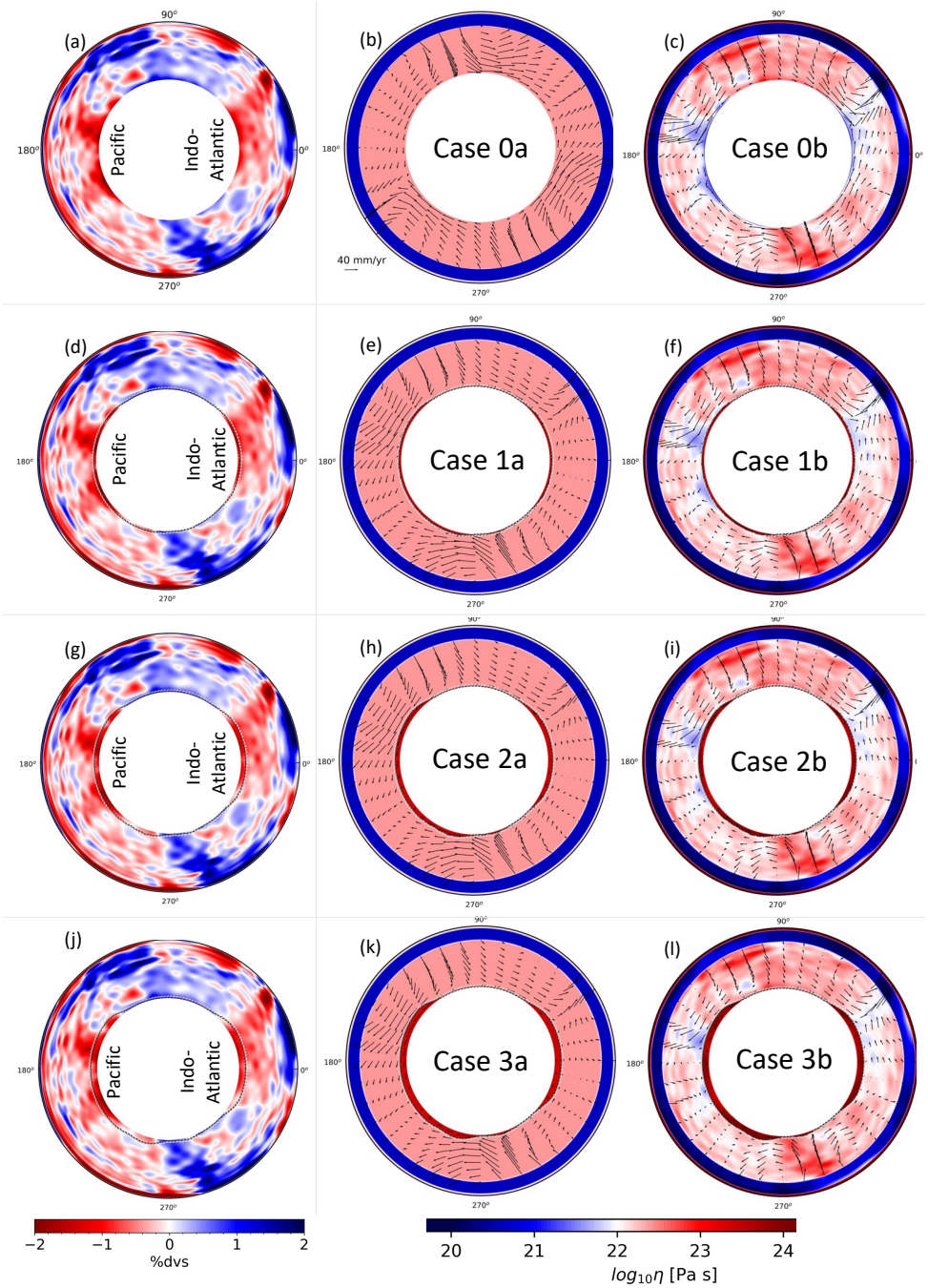

Figure 2. In the leftmost column is an equatorial slice of the seismic tomographic model S40RTS. Dashed lines show the LLSVP topography for the cases in the same row. Degrees of longitude are annotated around the outer circumference, and dashed lines show the LLSVP topography. In the middle and rightmost columns are the viscosity fields with velocity fields superposed as vectors.

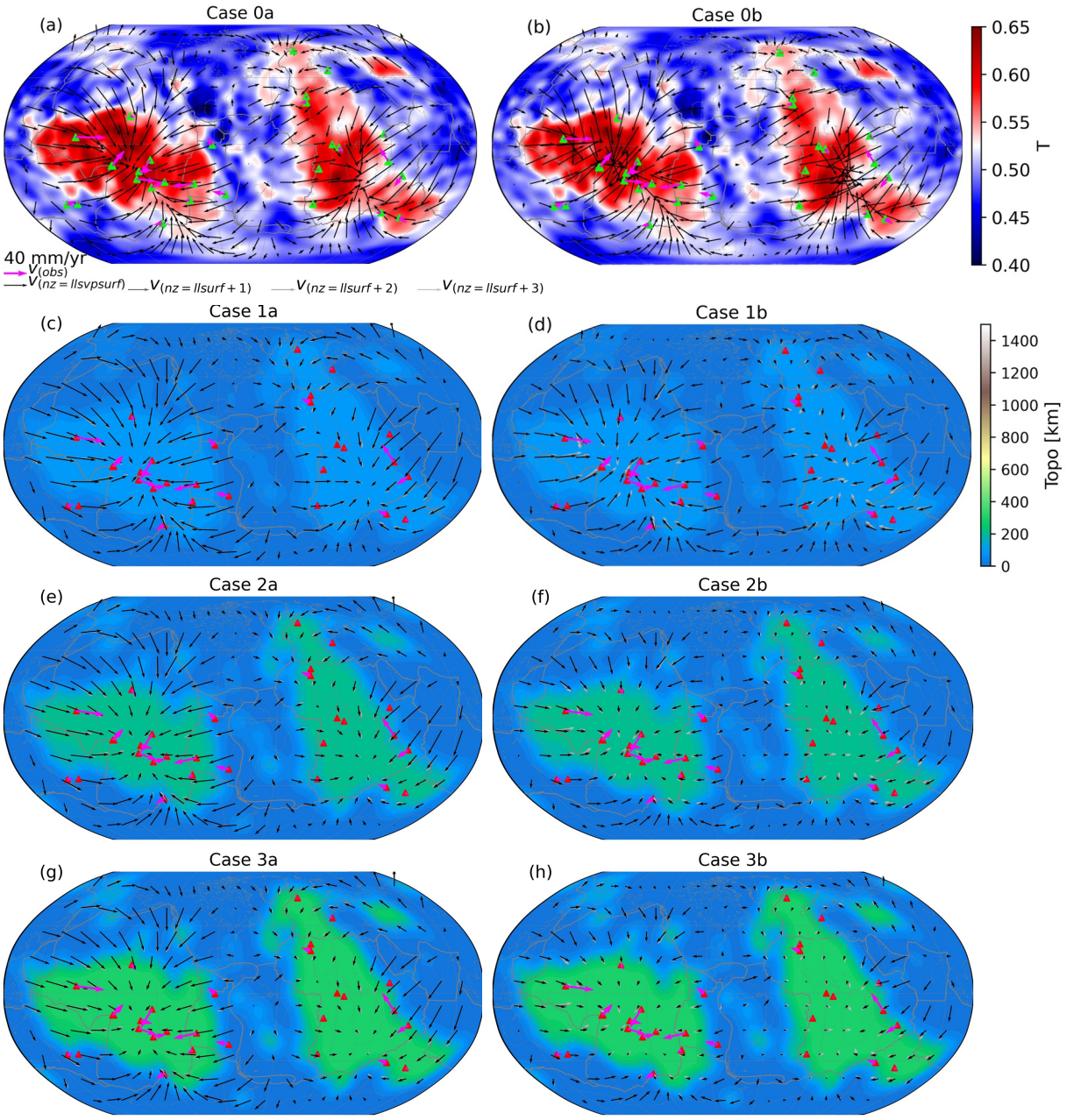

Figure 3. Temperature at 2850 km depth based on a uniform scaling of S40RTS, and basal velocity projected to the surface for Case 0a (a), and Case 0b (b), which treat LLSVPs as ambient mantle. Red and green triangles mark the surface locations of hotspots, and observed hotspot motions relative to the FHRF are plotted as magenta vectors. We present the LLSVP topography and velocity field on the CMB or LLSVP surface, projected radially to the surface as black vectors in Case 1a (c), Case 1b (d), Case 2a (e), Case 2b (f), Case 3a (g), and Case 3b (h). Grey vectors show velocity at nodes just above the LLSVP surface.

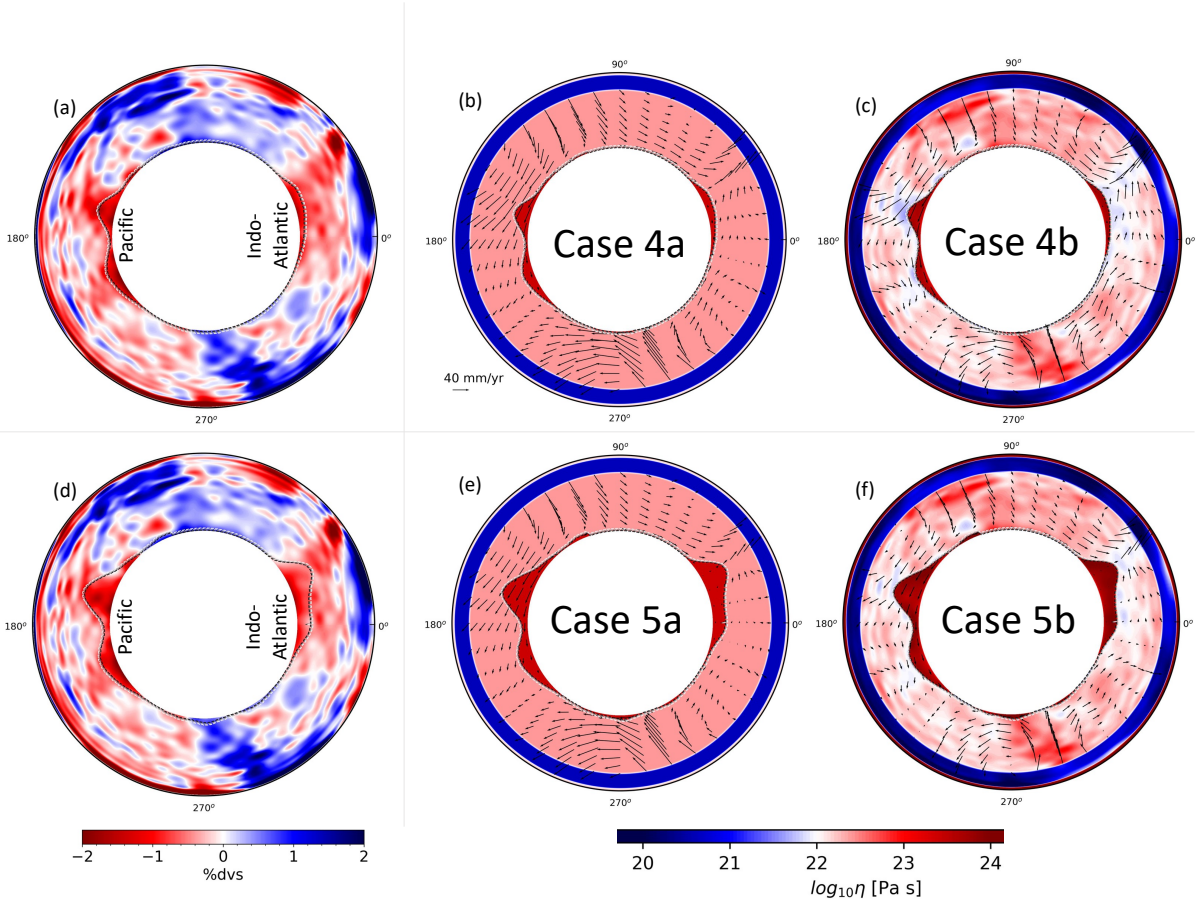

Figure 4. In the leftmost column is the seismic structure (S40RTS) with LLSVP topography superposed as dashed lines in the equatorial plane for Case 4a and 4b (a) and Case 5a and 5b (d). Degrees of longitude are marked on the outside circumference. In the middle and rightmost columns are the viscosity fields and velocity vectors for Case 4a (b) Case 4b (c), Case 5a (e), and Case 5b (f).

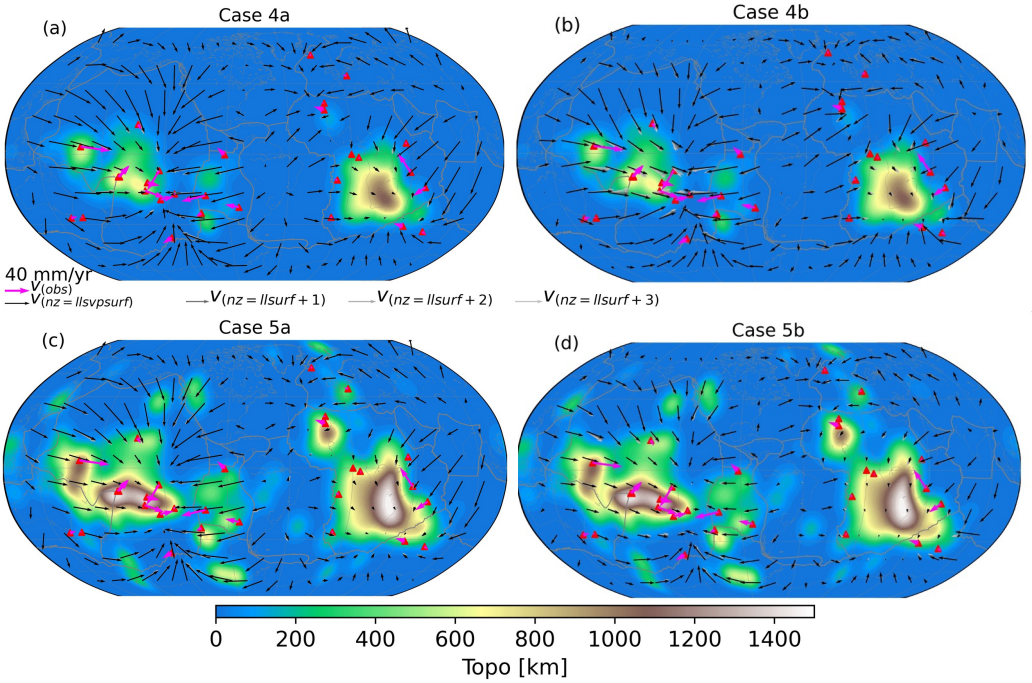

Figure 5. LLSVP topography with predicted basal velocity projected radially to the Earth's surface in Case 4a (a), Case 4b (b), Case 5a (c), and Case 5b (d). All other symbols are the same as in Figure 3.

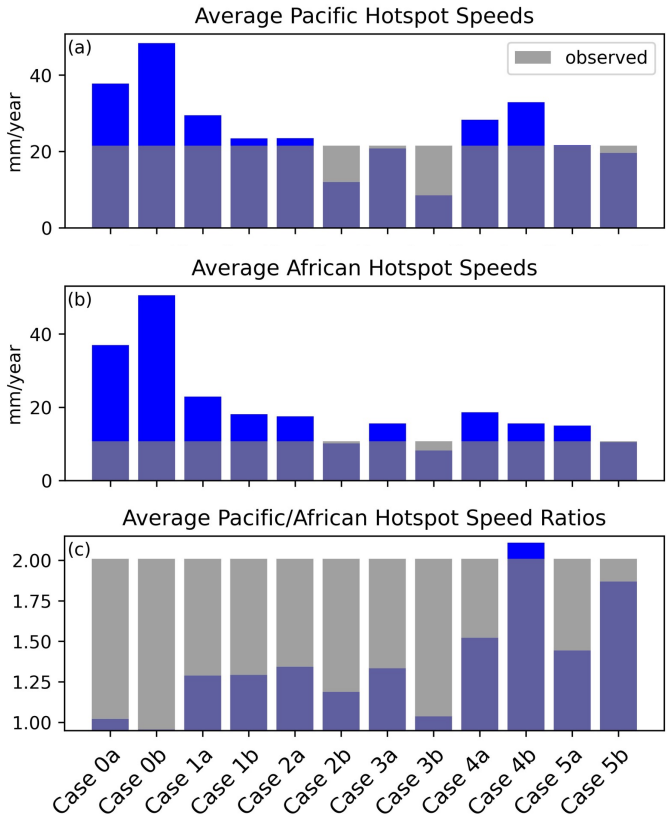

Figure 6. Mean hotspot speeds in the Pacific (a), Indo-Atlantic (b), and the ratio of the former to the latter (c). Model predictions are plotted in blue, and the observations relative to the FHRF are superposed in grey.

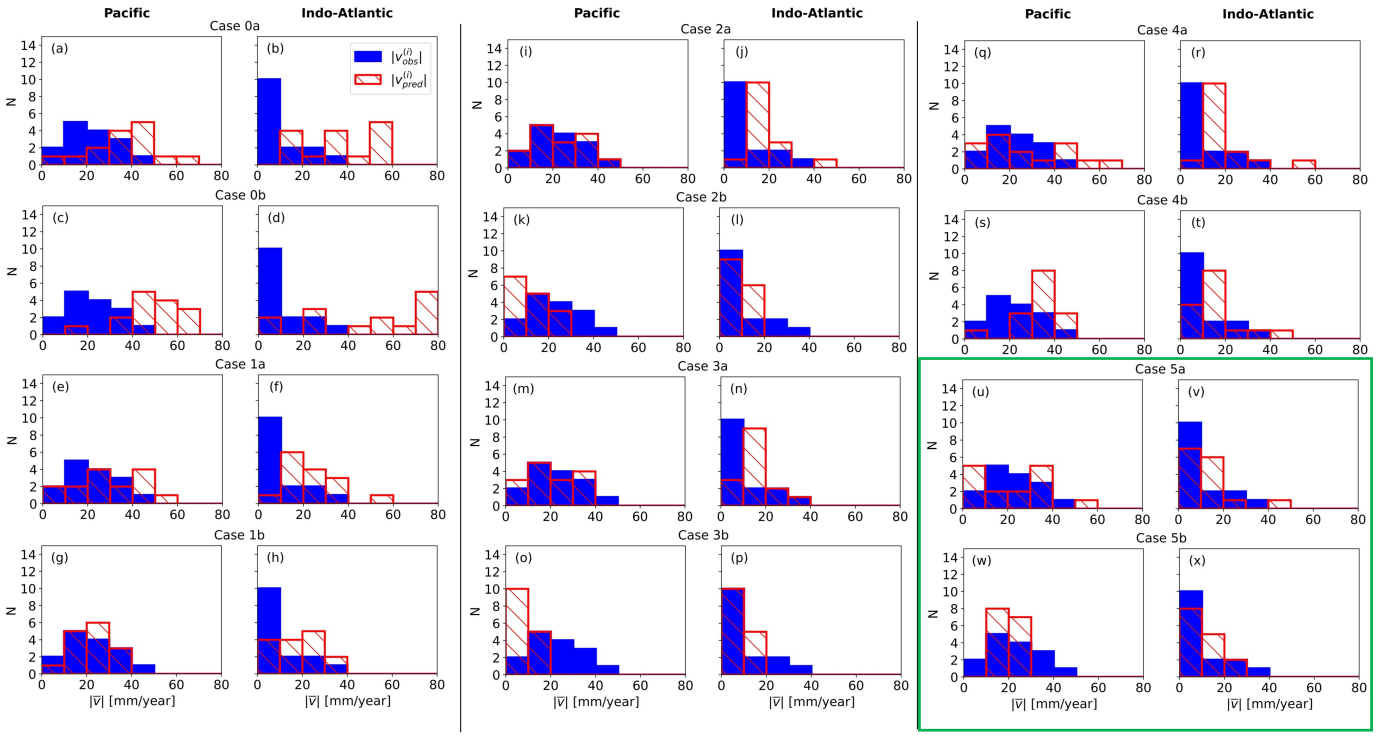

Figure 7. Observed and model hotspot speeds binned by 10 mm/yr increments, shown separately for the Pacific (left panels) and Indo-Atlantic (right panels) for each case (see titles). The observed distributions, relative to the FHRF, are plotted in solid blue. The predictions from each case are plotted as red and hatched.

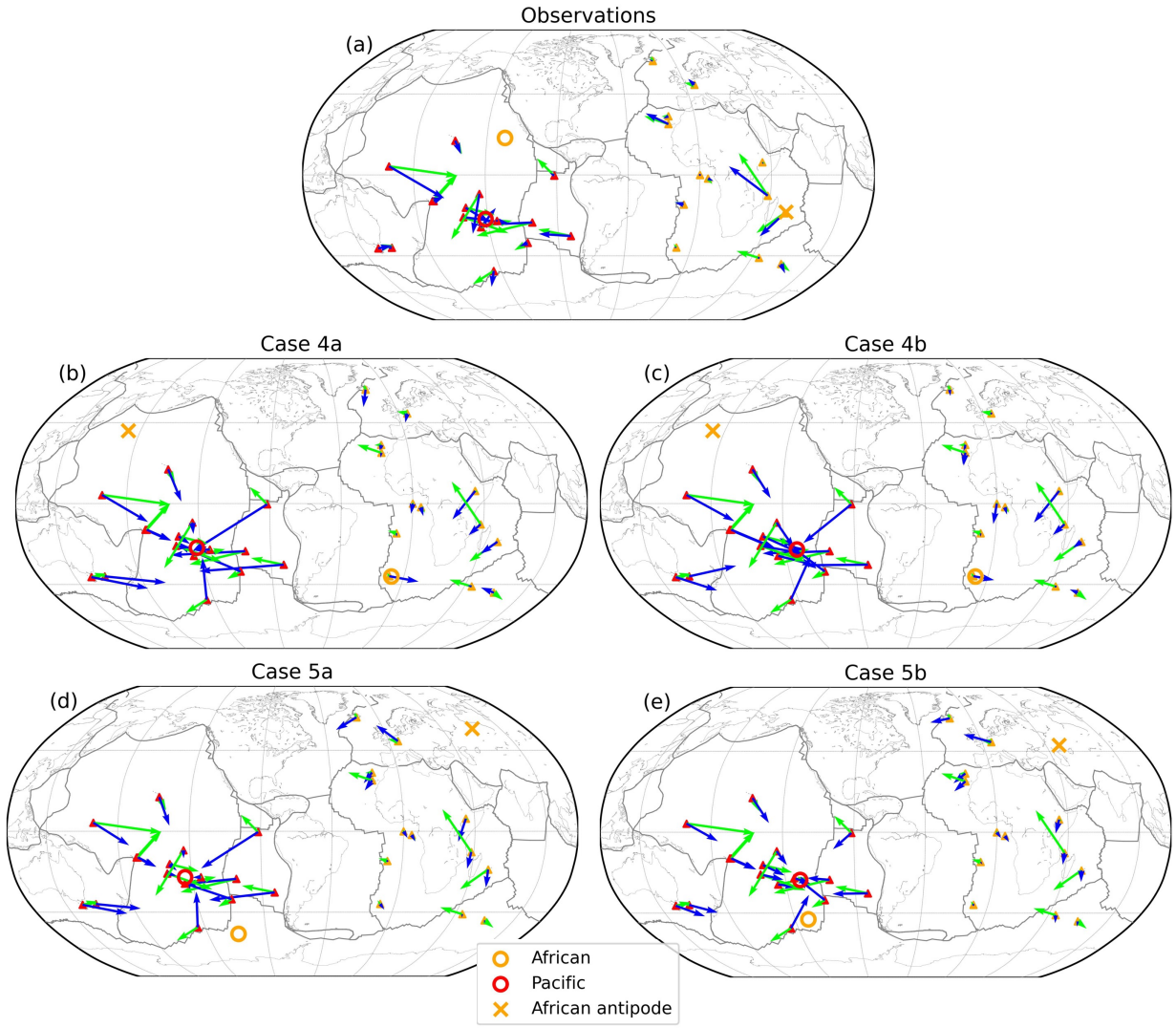

Figure 8. The points of maximum convergence for hotspot motions in the Pacific (red circles) and the Indo-Atlantic (yellow circles) based on observations relative to the FHRF (a), Case 4a (b), and Case 4b (c), Case 5a (d), and Case 5b (e). The Indo-Atlantic antipode is also shown since the point of maximum convergence sometimes lands in the Pacific hemisphere.

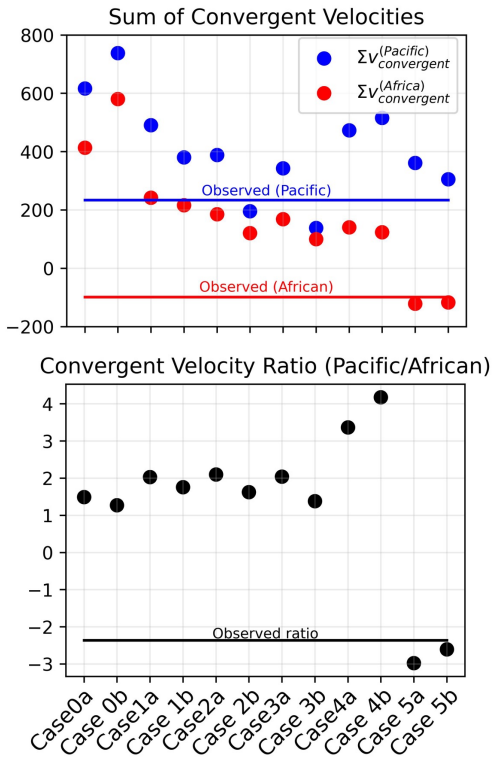

Figure 9. (a) The sum of convergent velocities (shown in map-view in Figure 8) and (b) the ratio of the sum of convergence velocities in the Pacific and Indo-Atlantic. Model predictions are plotted as dots, and observations relative to the FHRF as lines.

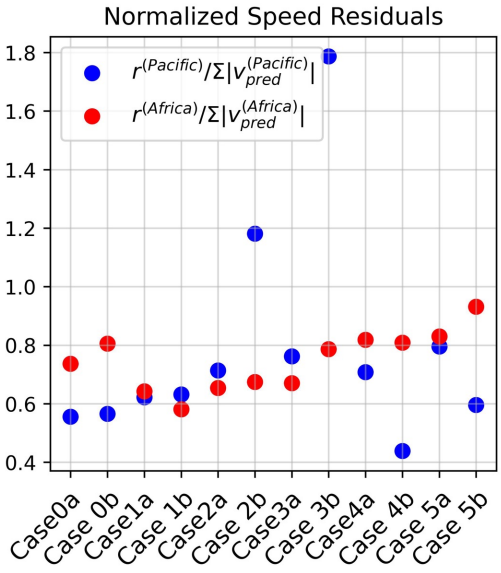

Figure 10. The residual speed (predictions minus observations) normalized by the predicted speed in the Pacific and Indo-Atlantic.

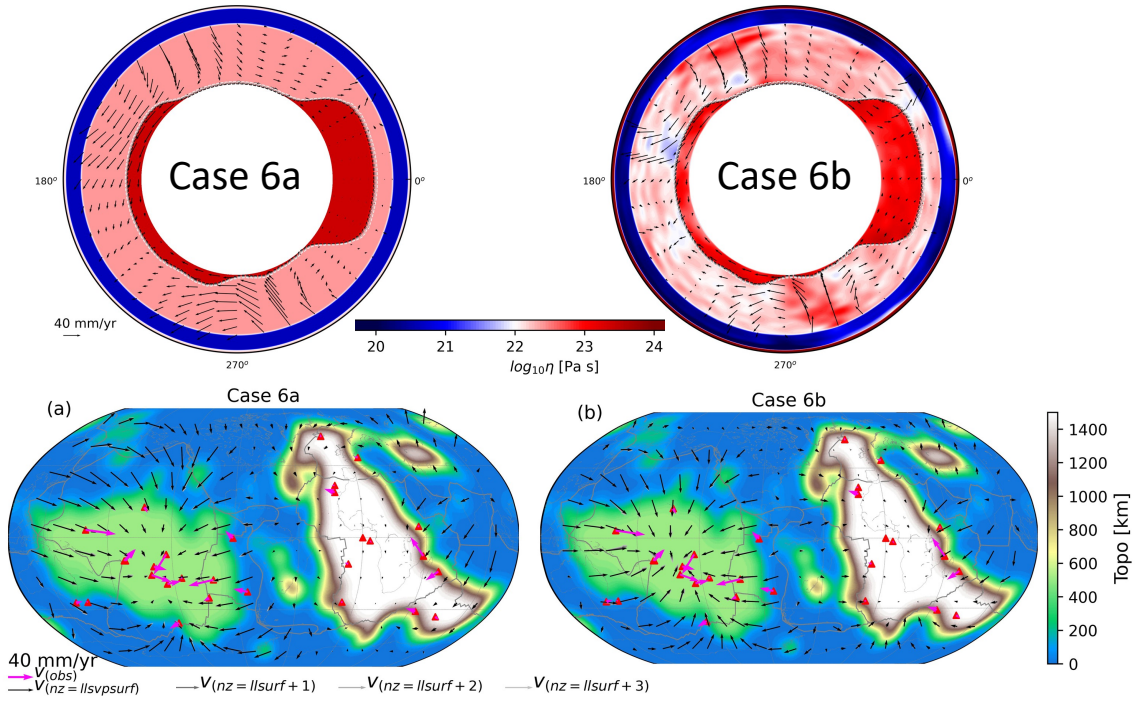

Figure 11. The viscosity fields and velocity vectors for Case 6a and Case 6b in the equatorial plane (top row). We also show the topography of the LLSVPs and the velocity vectors in map view (bottom row).